GPS Solutions (2024) 28:41
https://doi.org/10.1007/s10291-023-01581-8

ORIGINAL ARTICLE

Effects of BDS flex power on DCB estimation and PPP convergence

Zhou Wu[1] · Shuhui Li[1] · Hongxia Wan[2] · Ming Ji[1] · Pengrui Mao[1] · Shaojie Xiong[1]

Received: 11 August 2023 / Accepted: 10 November 2023 / Published online: 6 December 2023

Abstract

The flex power technology of satellite navigation systems can improve the anti-jamming ability of navigation signals, but the flex power technology may have many effects in navigation and positioning. In this paper, the effects of the BeiDou Navigation Satellite System (BDS) flex power on differential code biases (DCBs) estimation and precise point positioning (PPP) convergence were researched. First, the variation characteristics of the carrier-to-noise density ratio and daily DCB products during BDS flex power active periods were analyzed. Then, the influence of BDS flex power on DCB estimation was examined by different DCB estimation strategies. Finally, the convergence performance of PPP algorithms using different DCB corrections during BDS flex power active periods was investigated. Results show the B3I signals of the BDS-2 Geostationary Orbit (GEO), Medium Earth Orbit (MEO), and Inclined Geosynchronous Orbit (IGSO) satellites have the capability of flex power. The BDS observation data during flex power events that occurred on DOY 029 in 2021 were analyzed. Estimates derived from reference satellite constraint indicate that the DCB of the satellites without flex power activated did not change, whereas the DCB of the IGSO satellites with flex power activated increased by 10–15 ns. When the flex power was activated at part of the DOY 029, 2021, the correction of daily DCB products resulted in the extension of BDS PPP convergence time for most stations within the flex power coverage area, regardless of whether the flex power was activated; however, the convergence time of PPP was unaffected if the station was outside the flex power coverage area.

Keywords BDS · Flex power · Differential code biases · Precise point positioning

Introduction

With the development of modern satellite navigation systems and the continuous progress of related technologies, enhancing signal strength to improve the anti-jamming capability of navigation systems has become a popular research topic. Through the analysis of the carrier-to-noise density ratio (C/N_0) in global navigation satellite system (GNSS) observation data, the navigation signal enhancement phenomenon of Global Positioning System (GPS) and BeiDou Navigation Satellite System (BDS) can be detected, which is also known as flex power (Jiménez-Baños et al. 2010; Wang et al. 2022). The flex power technology of GPS has undergone early development and is considered mature, providing the ability to enhance coverage flexibly and systematically on a global scale (Yang et al. 2022; Esenbuğa et al. 2023). Compared with GPS, the flex power technology of BDS is still in the early stage. The flex power technology necessitates readjusting the RF output power of the satellites while enhancing the signal strength, which can affect differential code biases (DCBs), receiver-side observation data, and the performance of precise point positioning (PPP) services for clients (Esenbuğa and Hauschild 2020). Therefore, studying the influence of flex power has great importance for navigation systems.

Currently, extensive research is being conducted on the flex power of GPS, with a primary emphasis on mode classification, detection, and the analysis of associated influences. Given the mode classification of GPS flex power, Steigenberger (2019) summarized and classified early GPS flex power events and divided these flex power events into three modes according to their enhancement signal, enhancement amplitude, and satellite type. Esenbuğa et al. (2023) provided a more detailed classification of the modes

✉ Shuhui Li
li.shuhui@163.com

[1] School of Land Science and Technology, China University of Geosciences (Beijing), 29 Xueyuan Road, Haidian District, Beijing 100083, China

[2] China Satellite Network Innovation Co., Lid, No.5 Anding Road, Chaoyang District, Beijing 100029, China

of GPS flex power. They classified GPS flex power events that occurred before March 2022 into nine flex power modes. In addition to considering factors like enhancement signal, enhancement amplitude, and satellite type, the classification incorporated the ground track information of the satellites during the GPS flex power active periods. Aiming at the detection of GPS flex power, Li et al. (2022) proposed that global multi-station C/N_0 observation data could be used for detection. Yang et al. (2022) invented a real-time GPS flex power detection system based on machine learning, and the system can ensure the false alarm rate of real-time monitoring is less than 10^{-5} and the missed alarm rate is less than 10^{-3}. Tang et al. (2022) proposed a method to determine the precise relationship between the observed C/N_0 data and the actual power enhancement. For the related influence of GPS flex power, most previous studies focused on the influence of flex power on DCB. Steigenberger (2019) estimated the intra-frequency DCB of different GPS flex power modes based on the high-rate DCB estimation method, and the results showed GPS flex power caused the change of intra-frequency DCB. Xiang et al. (2020) analyzed the long-term stability of DCB and found that the average influence of GPS flex power on intra-frequency DCB is about 0.4 ns. Some subsequent studies proposed distinguishing DCB into two constants for estimation during flex power active periods and finally concluded the average influence of GPS flex power on intra-frequency DCB of L1 and L2 frequencies is about 0.3 ns, and the maximum influence can reach 0.9 and 0.7 ns, respectively; however, the influence on inter-frequency DCB is not substantial due to the influence of ionosphere estimation accuracy (Esenbuğa and Hauschild 2020; Esenbuga et al. 2020; Esenbuğa et al. 2023). In addition, Li et al. (2022) comprehensively analyzed and evaluated the coverage, the constellation performance, the relationship between signal enhancement amplitude and C/N_0, and the anti-jamming capability of GPS flex power.

Compared with the study on the flex power of GPS, studies on the flex power of BDS are few. Considering the change of the DCB estimation reference datum during BDS flex power active periods, Cui (2022) used the reference satellite constraint for high-rate BDS DCB estimation and concluded BDS flex power turning on can cause DCB change by 9–14 ns. Su and Jiao (2023) proposed a DCB estimation approach with high temporal resolution and analyzed the necessity of this method during BDS flex power active periods.

This paper focuses on the effects of BDS flex power on DCB estimation and PPP convergence and is organized as follows. The data utilized and the principles and strategies employed for DCB estimation and the PPP algorithm are introduced in the next section. Then, effects of BDS flex power are analyzed, with emphasis on its effects on DCB and PPP convergence time. After that, the comprehensive summary and conclusion are given.

Data and methods

This section introduces the network of reference stations used for DCB estimation and PPP convergence experiments and provides information on the sources of the relevant data. Subsequently, this section explains the principles of DCB estimation and PPP method, as well as the related strategies used in this paper.

Data

Observation data from 152 evenly distributed BDS IGS stations worldwide were utilized for DCB estimation. Among these stations, 80 stations were chosen for PPP convergence experiments. Figure 1 illustrates the distribution of these stations, with yellow triangles representing the 152 stations

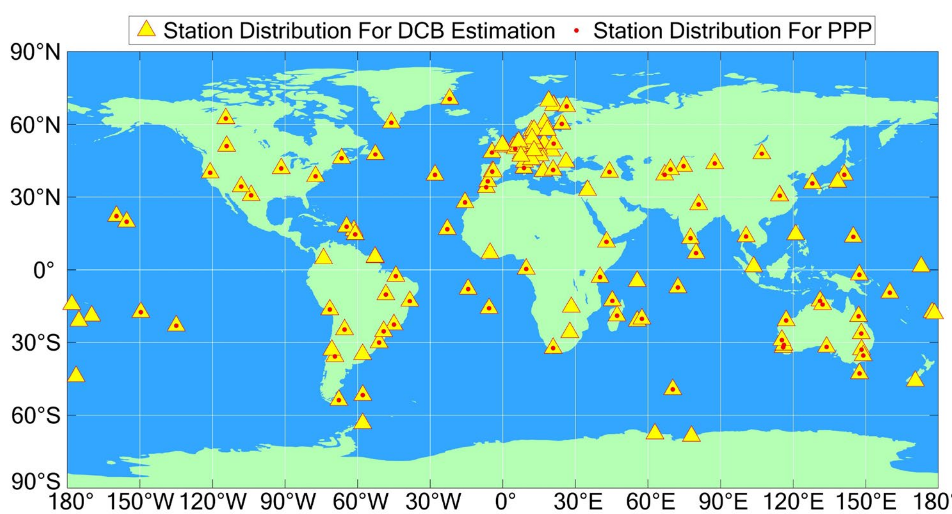

Fig. 1 Distribution of IGS stations for DCB estimation and PPP convergence analysis

utilized for DCB estimation and red dots indicating the 80 stations utilized for PPP convergence experiments. The observed data from all these stations included C2I and C6I measurements. DCB products provided by the Chinese Academy of Sciences (CAS) and the German Aerospace Center (DLR) were used for comparative analysis. Additionally, precise ephemeris, precise clock offsets, Global Ionospheric maps (GIM), and other relevant data files were utilized. All the data can be obtained from ftp://cddis.gsfc.nasa.gov/pub/.

Methods

The following section provides an exposition on the fundamental principles of DCB estimation and PPP, offering a detailed description of the DCB estimation strategy and PPP data processing strategy employed in this paper. These contents serve as the methodological basis for subsequent experimental analysis.

DCB estimation method

Typically, DCB can be estimated by utilizing the geometry-free linear combination of dual-frequency pseudorange observations. The geometry-free linear combination of the dual-frequency signal pseudorange observations is as follows:

$$\tilde{P}^s_{r,1} - \tilde{P}^s_{r,2} = 40.28 \cdot \left(\frac{1}{f_1^2} - \frac{1}{f_2^2}\right) \cdot STEC^s + DCB_{r,12} + DCB^s_{12} \tag{1}$$

where $\tilde{P}^s_{r,1}$ and $\tilde{P}^s_{r,2}$ represent the carrier phase smoothed pseudorange observations. The carrier phase smoothing pseudorange technique adjusts raw pseudorange observations using the change in carrier phase observations over a specific time interval, and it can greatly improve the accuracy of pseudorange observations without introducing ambiguity (Wang et al. 2016). f_1 and f_2 represent the frequencies of 1 and 2, respectively. $STEC^s$ represents the ionospheric delay on the inclined path. $DCB_{r,12}$ represents the receiver DCB. DCB^s_{12} represents the satellite DCB.

In Eq. (1), $STEC^s$ can be obtained using either GIM or function modeling. The accuracy of DCB estimation is influenced by the uneven distribution of BDS stations globally (Ren et al. 2020). Therefore, the method of using GIM interpolation to obtain ionospheric information was selected to compensate for the limited coverage of BDS stations and to improve the accuracy of DCB estimation. The DCB estimation for the receiver and the satellite was commonly assumed constant over 24 h (Li et al. 2018). In order to separate satellite DCB from receiver DCB, a zero-sum condition or a reference satellite constraint is usually imposed to eliminate rank deficiency in the observation equation (Montenbruck et al. 2014; Xiang et al. 2020). It is worth mentioning that the satellites with flex power activated are not suitable for use as the reference datum.

Due to the influence of flex power, considering the DCB of flex power satellites as a constant in the daily DCB estimate is no longer appropriate. Therefore, differentiating the DCB of flex power satellites into two distinct constants during flex power active periods is suggested (Esenbuğa and Hauschild 2020). In this paper, considering the on times of the BDS flex power are close, the midpoint as the dividing moment for the on or off of the flex power can be approximated. Consequently, a day of data can be divided into two periods, namely the flex power period and the non-flex power period, and the DCB for each period can be estimated separately. Generally, the variation of satellite DCB within a day is minimal. Therefore, the difference between the DCB of the two periods can be used to evaluate the effect of flex power on DCB.

In this paper, two different strategies for DCB estimation were employed to analyze the effect of BDS flex power. The specifics of the two strategies are outlined in Table 1. In the first strategy, the high-rate DCB estimation method was utilized to estimate a set of DCB every 15 min, and the separation of the receiver and satellite DCB followed the reference satellite constraint condition (Steigenberger 2019). This strategy aims to analyze the influence of the BDS flex power on the time series of DCB^{C19} time series over the course of a day. The superscript C19 of DCB means that the reference satellite is C19. In the second strategy, the receiver and satellite DCB was regarded as a constant within a day or divided into two periods for estimation, and the separation of the receiver and satellite DCB followed the reference satellite constraint condition. This strategy aims to analyze the differences between the estimated values of DCB^{C19}_{Ave}, DCB^{C19}_{Flex} and DCB^{C19}_{Nor} when BDS flex power is activated at part of a day. Here, the subscripts *Flex* and *Nor* represent the DCB corresponding to the flex power period and the non-flex power period, respectively; subscript *Ave* represents the DCB estimated as a constant in one day.

Table 1 Two different DCB estimation strategies

Strategies name	DCB estimation times	Constraint condition	DCB estimate results
Strategy 1	15 min	Reference satellite	DCB^{C19} time series
Strategy 2	One day two periods	Reference satellite	$DCB^{C19}_{Ave}/DCB^{C19}_{Flex}$, DCB^{C19}_{Nor}

PPP mode and strategies

The original PPP observation equations for BDS are as follows (Zhou 2018):

$$P^s_{r,j} = \rho^s_r + C \cdot \left(dt_r - dt^s\right) + \mu_j \cdot I^s_{r,1} + T^s_r + C \cdot (d_{r,j} - d^s_j) + \varepsilon^s_{p,j} \quad (2)$$

$$L^s_{r,j} = \rho^s_r + C \cdot \left(dt_r - dt^s\right) - \mu_j \cdot I^s_{r,1} + T^s_r + \lambda_{r,j} \cdot \left(N^s_{r,j} + b_{r,j} - b^s_j\right) + \xi^s_{p,j} \quad (3)$$

where $P^s_{r,j}$ and $L^s_{r,j}$ represent the pseudorange and carrier phase observation, respectively; superscripts and subscripts s, r, and j indicate they are related to the satellite, the receiver, and the signal frequencies f_1 and f_2, respectively; C is the speed of light in a vacuum; dt_r and dt^s represent the clock offset of the receiver and satellite, respectively; $I^s_{r,1}$ represents the ionospheric delay at frequency f_1; μ_j represents the frequency-dependent ionospheric delay amplification factor ($\mu_j = f_1^2/f_2^2$); T^s_r represents the tropospheric delay in the propagation path; $d_{r,j}$ and d^s_j represent the uncalibrated code delays of the receiver and the satellite, respectively; and $N^s_{r,j}$ represents the integer ambiguity corresponding to frequency f_j;$b_{r,j}$ and b^s_j represent the uncalibrated phase delays of the receiver and the satellite, respectively; $\varepsilon^s_{p,j}$ and $\xi^s_{p,j}$ represent the sum of the observed noise, multipath effects, and other unmodeled errors of the pseudorange and the carrier phase, respectively.

For the original observation equations in Eqs. (2) and (3), this study employed an undifferenced and uncombined model for BDS PPP data processing. The undifferenced and uncombined model originates from the original observed equations without incorporating any form of combination. The parameters to be estimated in this model are outlined as follows (Zhou et al. 2019):

$$X = [x, y, z, dt_r, I^s_{r,1}, ZWD_r, N^s_{r,1}, N^s_{r,2}] \quad (4)$$

where x, y, and z represent the 3D coordinates to be estimated; dt_r represents the receiver clock offset; $I^s_{r,1}$ represents the ionospheric delay on frequency 1; ZWD_r represents the zenith wet delay; and $N^s_{r,1}$ and $N^s_{r,2}$ represent the ambiguities on frequencies 1 and 2, respectively.

A PPP convergence experiment was conducted using Net_Diff software, and the specific data processing strategies of PPP are presented in Table 2.

BDS flex power effect analysis

This section begins by describing the variation characteristics of C/N_0 and DCB products during BDS flex power active periods. Subsequently, this section analyzes the influence of flex power on DCB estimation, using different estimation strategies. Finally, this section determines the effect of flex power on PPP convergence time through PPP convergence experiments with various DCB corrections.

Table 2 Data processing strategies for PPP

Options	Processing strategies
System	BDS
PPP model	Undifferenced and uncombined
Data processing software	Net_Diff (Mou et al. 2023)
Observation interval	30 s
Frequency	B1I, B3I
Estimator	Kalman filtering
Elevation	7°
Weight allocation of observations	Elevation model, $a^2 + b^2/sin^2(ele)$
Satellite phase center correction	IGS14_2196.atx
Receiver phase center correction	IGS14_2196.atx
Satellite orbit and clock	WUM precise satellite orbit and clock offset
Tropospheric delay	Model correction + Random walk
Ionospheric delay	GIM constraint + white noise estimation
Receiver coordinate	The constant of a day
Ambiguity	Float
Receiver clock offset	Random walk
ISB	Random walk (Estimated BDS-2 and BDS-3 ISB)
DCB correction	Daily DCB products (CAS)
Definition of convergence	The error is less than 0.1 m in the E, N, and U directions for at least 20 epochs

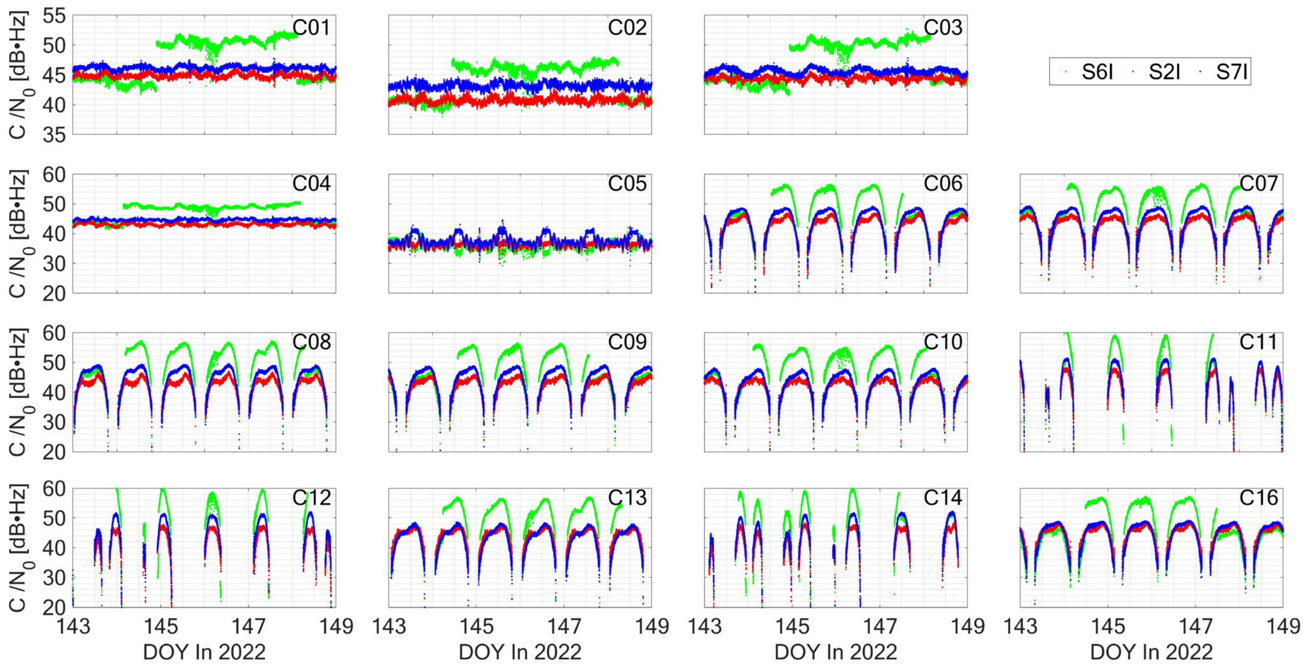

Fig. 2 Satellite C/N_0 of GAMG station during DOY 143–148 in 2022

Table 3 BDS satellite flex power on and off time during DOY 143–148 in 2022

PRN	Flex power on and off time (UT/DOY)	PRN	Flex power on and off time (UT/DOY)
C01	21:41:30/144–02:40:30/148	C09	13:44:00/144–13:40:30/147
C02	10:41:30/144–05:40:30/148	C10	02:44:00/144–01:40:30/148
C03	22:41:30/144–03:40:30/148	C11	00:44:00/144–09:40:30/147
C04	03:41:30/144–04:40:30/148	C12	23:44:00/143–08:40:30/148
C06	12:44:00/144–12:40:30/147	C13	05:44:00/144–07:40:30/148
C07	01:44:00/144–00:40:30/148	C14	18:44:00/143–10:40:30/147
C08	04:44:00/144–06:40:30/148	C16	11:44:00/144–11:40:30/147

C/N_0 and daily DCB products

The BDS flex power event occurring at DOY 143–148 in 2022 was analyzed. During this event, there were more BDS satellites with flex power activated. The C/N_0 values for the S2I, S6I, and S7I of the GAMG station were extracted, as depicted in Fig. 2. The full name of the GAMG station is GAMG00KOR, which is an IGS station located in South Korea. In Fig. 2, all BDS-2 satellites, except C05, demonstrated flex power on the B3I signal. Their C/N_0 on S6I increased by 6–10 dB during DOY 143–148, 2022. According to the variation in C/N_0, Table 3 presents detailed information on the obtained BDS flex power event. Examining Fig. 2 and Table 3 reveals the majority of satellites that exhibited activated flex power were Inclined Geosynchronous Orbit (IGSO) satellites of BDS-2, so the main coverage range of flex power for this occasion is in the Asia–Pacific region.

Table 4 Extracted DCB types and related information regarding BDS B3I

Extracted types of DCB	Institution	Satellite types
C2I-C6I	CAS, DLR	BDS-2 and BDS-3
C1X-C6I	CAS	BDS-3
C1P-C6I	CAS	BDS-3

To analyze the relationship between BDS flex power and the changes in daily DCB products, the DCB products related to the B3I signal released by CAS and DLR were extracted here. The extracted DCBs and their corresponding information are presented in Table 4.

Figure 3 depicts the variations in C2I–C6I DCB during DOY 120–160 in 2022 for satellites with flex power activated. The DCB data released by both institutions reveal substantial changes in the DCB of all satellites with flex power activated during DOY 143–148. However, the effect of flex power on DCB changes differed among different satellite types. Specifically, in Fig. 3a and b, the C2I–C6I DCB values of Geostationary Orbit (GEO) satellites decreased by 6–10 ns, whereas in Fig. 3c and d, the C2I–C6I DCB values of IGSO and Medium Earth Orbit (MEO) satellites increased by 5–14 ns. In addition, the C2I–C6I daily DCB products of these satellites with flex power activated did not mutate on the same day, and the specific change time coincided with the activation time of flex power, as specified in Table 3.

Figure 4 illustrates the changes in C2I–C6I, C1X–C6I, and C1P–C6I DCB during DOY 120–160 for satellites without the flex power activated. In Fig. 4a and b, the C2I–C6I DCB of the satellites without the flex power activated decreased by 1–2 ns during DOY 143–148, indicating a smaller amplitude and a higher similarity of change compared with the satellites with the flex power activated. These changes closely resembled the daily DCB products resulting from satellite replacement (Zhong et al. 2015; Xiang et al. 2020). Cui (2022) suggested the DCB variation in satellites without flex power activated is caused by changes in the reference datum before and after the DCB change and proposed to use the reference satellite constraint condition to minimize the effect of reference datum change. In Fig. 4c and d, the C1X–C6I and C1P–C6I DCB of the satellites without the flex power activated provided by CAS remained constant. Despite these DCBs including the B3I signal, CAS utilized a zero-mean constraint condition in estimating these DCBs, which did not involve any satellite with the flex power activated. Therefore, the reference datum was not affected by the flex power.

DCB estimation

The BDS flex power event occurring at DOY 029 in 2021 was analyzed to investigate the influence of BDS flex power on DCB estimation, since the flex power on times of

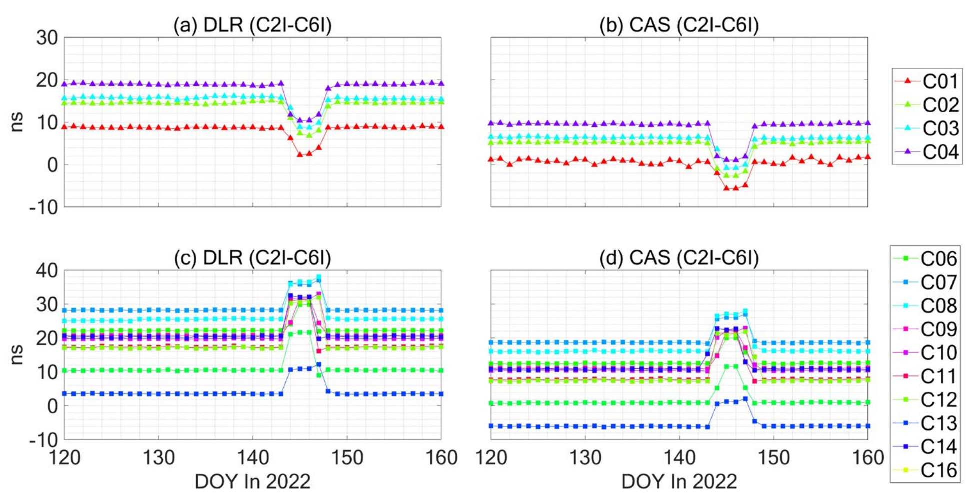

Fig. 3 C2I–C6I DCB of satellites with flex power activated released by CAS and DLR during DOY 120–160 in 2022

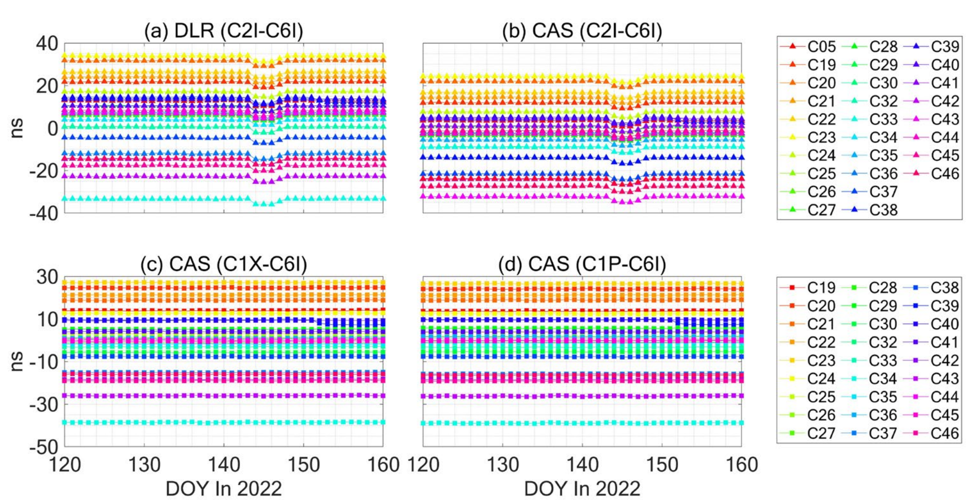

Fig. 4 C2I–C6I, C1X–C6I, and C1P–C6I DCB of satellites without flex power activated released by CAS and DLR during DOY 120–160 in 2022

different satellites was relatively close during this event. The details of BDS flex power activation on DOY 029 are presented in Table 5. All the satellites with flex power activated belong to the IGSO, and their flex power activation times were similar, which was convenient for data processing. The absence of C03 precision ephemeris on DOY 029 resulted in the exclusion of the C03 satellite from the DCB estimation.

High-rate DCB estimation

The high-rate DCB estimation method evaluates a set of DCBs every 15 min. By using the observation data of 152 globally dispersed BDS stations on DOY 029, 2021, the DCB^{C19} time series results obtained using DCB estimation strategy 1 under the reference satellite constraint condition of satellite C19 are shown in Fig. 5. During this period, flex power was not activated for satellite C19. The high-rate DCB time series of six satellites with flex power activated are shown in Fig. 5a. The DCB^{C19} time series of these satellites exhibited instantaneous changes at 07:45UT, 08:45UT, and 09:45UT. Excluding the difference in sampling rate, the DCB^{C19} change time of each satellite corresponded to the activation time of flex power in Table 5, and the magnitude of DCB^{C19} changes was approximately 8–14 ns. The DCB^{C19} time series of C01, C25, and C40 satellites without flex power activated are depicted in Fig. 5b. These DCBs were not affected by flex power and did not exhibit significant change corresponding to the three moments.

Table 5 BDS satellite flex power on-time on DOY 029, 2021

PRN	On-time (UT/DOY)	PRN	On-time (UT/DOY)
C07	07:43:30/029	C10	08:43:30/029
C08	09:43:30/029	C13	09:43:30/029
C09	08:43:30/029	C16	07:43:30/029

Daily DCB estimation

In this part, Strategy 2 was employed to analyze DCB estimation during the BDS flex power active periods. In this strategy, DCB was regarded as a constant within a day or divided into two periods for estimation under the reference satellite constraint condition of satellite C19. DCB_{Flex}^{C19} and DCB_{Nor}^{C19} represent the results of the flex power period and the non-flex power period, respectively. DCB_{Ave}^{C19} represents the result of estimating DCB as a constant within a day. As all satellites on DOY 029, 2021 exhibited a flex power activation time difference within 2 h in Table 5, and the intermediate time 08:43:30 UT was taken as the time to determine whether the flex power was activated.

Figures 6 and 7 show the results of DCB_{Flex}^{C19}, DCB_{Nor}^{C19}, and DCB_{Ave}^{C19} on DOY 029, 2021 estimated with reference satellite constraint. It is evident from Fig. 6 that the values of DCB_{Flex}^{C19} exhibited large differences from DCB_{Nor}^{C19} for the satellites with flex power activated. However, the values of DCB_{Flex}^{C19}, DCB_{Nor}^{C19}, and DCB_{Ave}^{C19} for the satellites without the flex power activated are almost equal in Fig. 7. Table 6 displays the difference between DCB_{Flex}^{C19} and DCB_{Nor}^{C19} estimated using the reference satellite constraint. The DCB difference for the six satellites with flex power activated ranged from 10 to 15 ns, whereas those for the satellites without flex power activated ranged from 0 to1 ns.

Figure 8 displays the results of $DCB_{Flex}^{C19} - DCB_{Ave}^{C19}$ and $DCB_{Nor}^{C19} - DCB_{Ave}^{C19}$ on DOY 029, 2021. For six IGSO satellites with flex power activated, $DCB_{Flex}^{C19} - DCB_{Ave}^{C19}$ ranged from 2 to 8 ns, and $DCB_{Nor}^{C19} - DCB_{Ave}^{C19}$ ranged from −6 to −10 ns. As for the satellites without flex power activated, their differences ranged from −1 to 1 ns. In summary, during BDS flex power active periods, the results obtained from the method that assumed a constant DCB demonstrated apparent disparities compared with DCB_{Flex}^{C19} and DCB_{Nor}^{C19}.

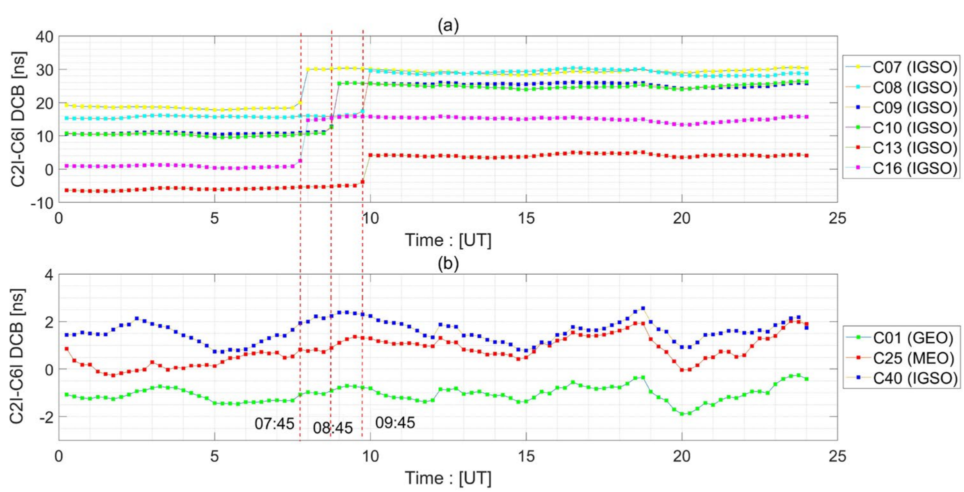

Fig. 5 High-rate estimation results DCB^{C19} on DOY 029, 2021

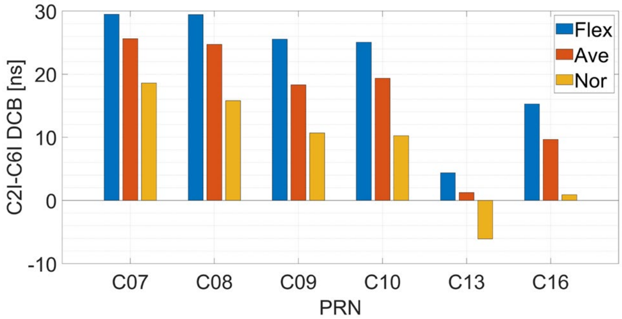

Fig. 6 Estimation results of DCB_{Flex}^{C19}, DCB_{Nor}^{C19}, and DCB_{Ave}^{C19} of satellites with flex power activated under the reference satellite constraint based on data from 152 BDS worldwide stations on DOY 029, 2021

PPP convergence

The correction of DCB has a negligible effect on the positioning accuracy of PPP after convergence, but it considerably influenced the convergence time of PPP (Dai et al. 2021; Ge et al. 2017; Guo et al. 2015). Therefore, this paper focused solely on PPP convergence time. To analyze the effects of BDS flex power on PPP convergence, experiments 1 and 2 were designed. A total of 80 BDS worldwide stations were selected, and the observation data on DOY 029, 2021 were analyzed. The specific schemes are shown in Table 7. For the DCB correction in experiments 1 and 2, the results of DCB estimation (DCB_{Flex}^{C19} and DCB_{Nor}^{C19}) from strategy 2 were used. Additionally, the CAS DCB product (DCB_{029}) from DOY 029 was used. The results of station distribution are shown in Fig. 9, where the color depth of

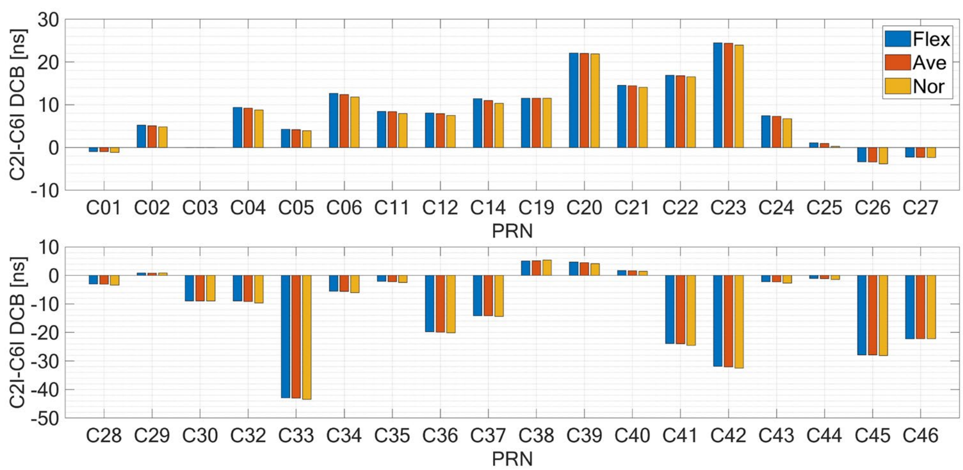

Fig. 7 Estimation results of DCB_{Flex}^{C19}, DCB_{Nor}^{C19}, and DCB_{Ave}^{C19} of satellites without flex power activated under the reference satellite constraint based on data from 152 BDS worldwide stations on DOY 029, 2021

Table 6 Difference between DCB_{Flex}^{C19} and DCB_{Nor}^{C19} of C2I-C6I from the reference satellite constraint based on data from 152 BDS worldwide stations on DOY 029, 2021

PRN	$DCB_{Flex}^{C19}-DCB_{Nor}^{C19}$ [ns]	PRN	$DCB_{Flex}^{C19}-DCB_{Nor}^{C19}$ [ns]	PRN	$DCB_{Flex}^{C19}-DCB_{Nor}^{C19}$ [ns]
C01	0.19	C19	–	C34	0.51
C02	0.37	C20	0.20	C35	0.42
C03	–	C21	0.49	C36	0.31
C04	0.62	C22	0.36	C37	0.17
C05	0.33	C23	0.53	C38	−0.33
C06	0.85	C24	0.72	C39	0.57
C07	10.93	C25	0.78	C40	0.30
C08	13.66	C26	0.49	C41	0.70
C09	14.88	C27	0.09	C42	0.66
C10	14.82	C28	0.41	C43	0.48
C11	0.49	C29	0.01	C44	0.39
C12	0.56	C30	0.05	C45	0.21
C13	10.42	C31	–	C46	−0.08
C14	1.10	C32	0.72	–	–
C16	14.34	C33	0.48	–	–

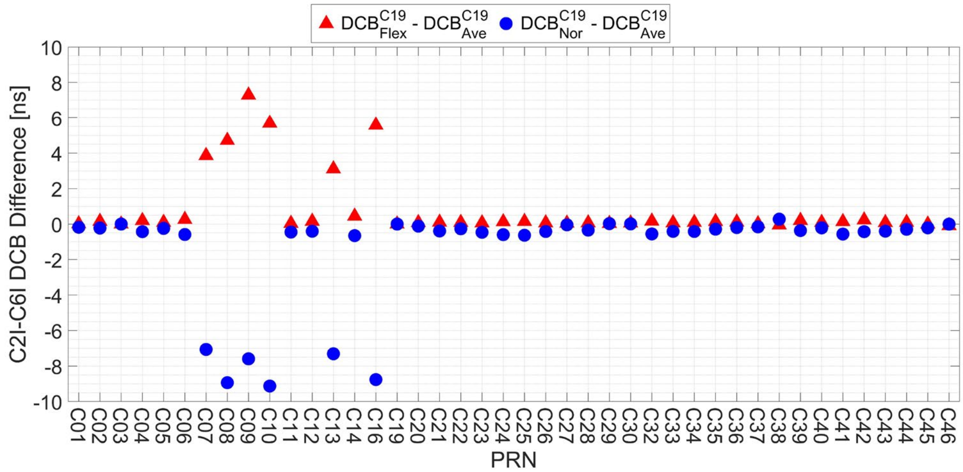

Fig. 8 The results of DCB^{C19}_{Flex}-DCB^{C19}_{Ave} and DCB^{C19}_{Nor}-DCB^{C19}_{Ave} by using data from 152 BDS worldwide stations on DOY 029, 2021

Table 7 Schemes for PPP convergence experiments

Experiment	Station area	Number of stations	DCB correction
Experiment 1: PPP convergence before activation of all satellites' flex power (00:00UT–04:00UT)	Flex power covered	40	DCB^{C19}_{Nor},DCB_{029}
	Flex power not covered	40	DCB^{C19}_{Nor},DCB_{029}
Experiment 2: PPP convergence after activation of all satellites' flex power (20:00UT–24:00UT)	Flex power covered	40	DCB_{029},DCB^{C19}_{Flex}
	Flex power not covered	40	DCB_{029},DCB^{C19}_{Flex}

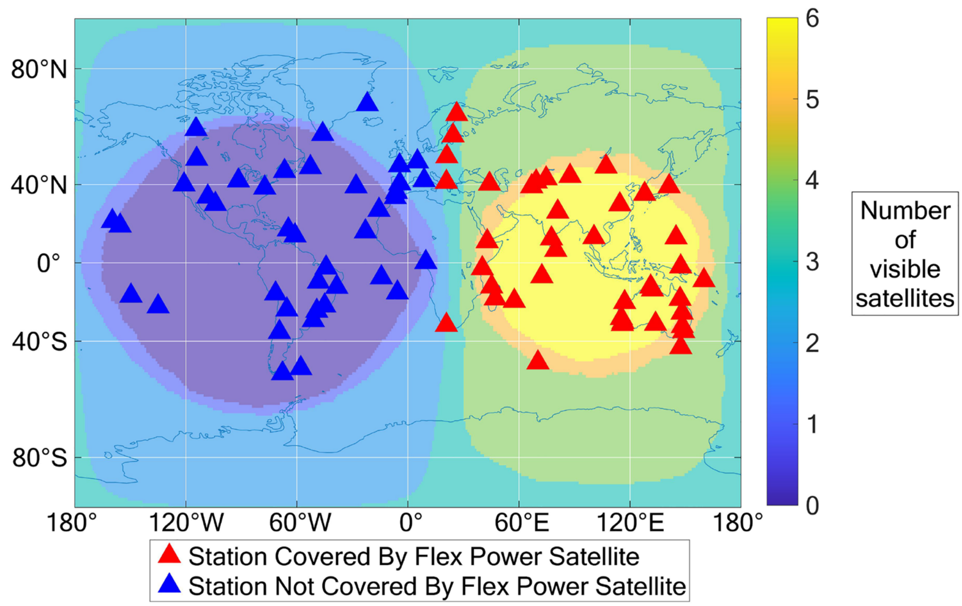

Fig. 9 Global distribution of stations in BDS PPP convergence experiments

the regions represented the visibility of 6 IGSO satellites with flex power activated. The red triangles represent the 40 stations covered by flex power, whereas the blue triangles represent the 40 stations outside the coverage area of flex power.

Experiment 1: PPP convergence before activation of all satellites' flex power

In experiment 1, the data selected for analysis were from 00:00 UT to 04:00 UT on DOY 029, 2021. During this period, flex power was not activated for any satellites. The DCB^{C19}_{Nor} and DCB_{029} corrections were applied to the stations

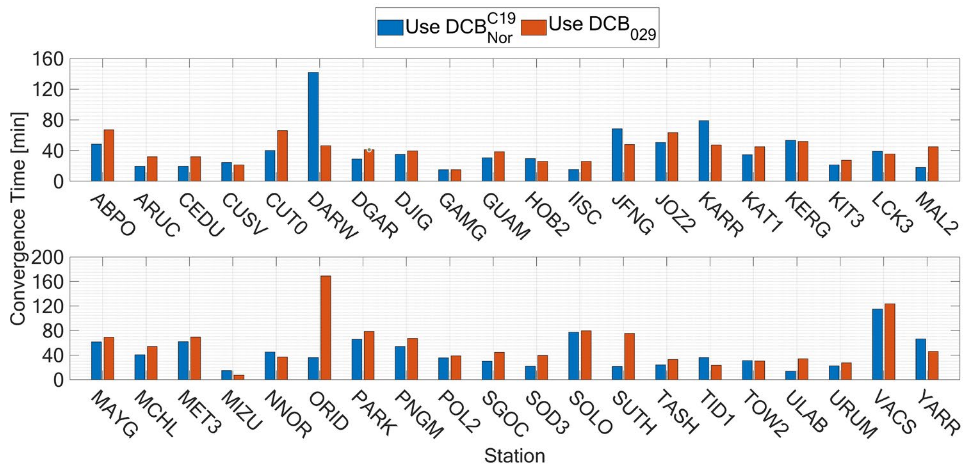

Fig. 10 Convergence time of BDS PPP corrected by DCB_{Nor}^{C19} and DCB_{029} for the stations within the flex power coverage area and data time from 00:00UT to 04:00UT on DOY 029, 2021

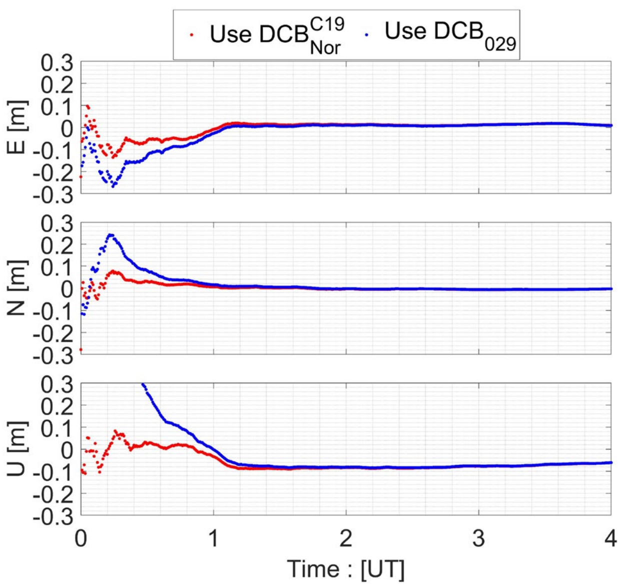

Fig. 11 BDS PPP convergence graphs for the MAL2 station in the E, N, and U directions corrected by DCB_{Nor}^{C19} and DCB_{029} and data time from 00:00UT to 04:00UT on DOY 029, 2021

within and outside the BDS flex power coverage area to compare the BDS PPP convergence time for different DCB corrections. Figure 10 displays the BDS PPP convergence time for each station within the BDS flex power coverage area, and the DCB corrections were made using DCB_{Nor}^{C19} and DCB_{029}. The results show that most stations BDS PPP converged faster by using DCB_{Nor}^{C19} corrected in the flex power coverage area. Figure 11 illustrates the BDS PPP convergence diagram for station MAL2 within the BDS flex power coverage area. The outcomes indicated that station MAL2 experienced faster convergence of the BDS PPP in the east (E), north (N), and up (U) directions when corrected using DCB_{Nor}^{C19}. Figure 12 depicts the BDS PPP convergence time corrected by DCB_{Nor}^{C19} and DCB_{029} for stations outside the BDS flex power coverage area. The results revealed that for the majority of stations outside the flex power coverage area, the convergence time of BDS PPP was the same when corrected by DCB_{Nor}^{C19} and DCB_{029}, and only a few stations exhibited differences in convergence time.

Table 8 presents the percentage of stations that exhibited faster convergence in PPP when corrected with DCB_{Nor}^{C19} and DCB_{029} within and outside the BDS flex power coverage

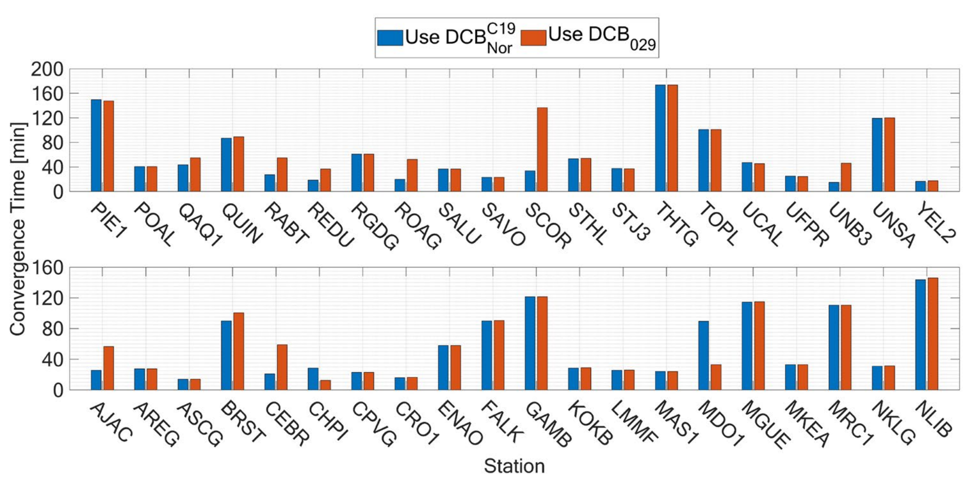

Fig. 12 Convergence time of BDS PPP corrected by DCB_{Nor}^{C19} and DCB_{029} for the stations outside the flex power coverage area and data time from 00:00UT to 04:00UT on DOY 029, 2021

Table 8 Number and percentage of stations exhibited faster convergence of BDS PPP using DCB_{Nor}^{C19} and DCB_{029} correction in different regions on DOY 029, 2021

Convergence faster DCB used	Flex power covered		Flex power not covered	
	Number of stations	Percentage	Number of stations	Percentage
Using DCB_{Nor}^{C19}	27	67.5%	12	30.0%
Using DCB_{029}	11	27.5%	4	10.0%
Same	2	5.0%	24	60.0%

Table 9 Maximum, minimum, and average convergence time improvement for stations within the flex power coverage area that showed faster convergence with PPP corrected by DCB_{Nor}^{C19} on DOY 029, 2021

Max		Min		Average
Station	Value [min]	Station	Value [min]	Value [min]
ORID	− 133.0	SOLO	− 2.0	− 17.9

area. The results indicated that within the flex power coverage area, 67.5% of the stations experienced faster convergence of BDS PPP when corrected by DCB_{Nor}^{C19}. However, outside the flex power coverage area, 60.0% of the stations exhibited the same convergence time for BDS PPP when corrected by DCB_{Nor}^{C19} and DCB_{029}. Table 9 provides statistics on the maximum, minimum, and average convergence time improvement for 27 BDS stations that showed faster convergence with PPP corrected by DCB_{Nor}^{C19}. The results indicated an average improvement in convergence time of around 17.9 min.

Experiment 2: PPP convergence after activation of all satellites' flex power

In experiment 2, the data selected for analysis were from 20:00 UT to 24:00 UT on DOY 029, 2021. During this period, the flex power of six IGSO satellites was activated. The DCB_{Flex}^{C19} and DCB_{029} corrections were applied to the stations within and outside the BDS flex power coverage area to compare the BDS PPP convergence time of different DCB corrections. Figure 13 displays the BDS PPP convergence time corrected by DCB_{Flex}^{C19} and DCB_{029} for stations within the BDS flex power coverage area. Since the PPP solution of the MCHL station data did not converge, the data for this station were not shown in the figure. The results were similar to Experiment 1, and most stations within the flex power coverage area converged faster by using DCB_{Flex}^{C19}. Figure 14 illustrates the BDS PPP convergence diagram for station KAT1 within the BDS flex power coverage area. The outcomes indicated station KAT1 experienced faster convergence of the BDS PPP in the E, N, and U directions when corrected using DCB_{Flex}^{C19}. Figure 15 depicts the BDS PPP convergence time corrected by DCB_{Flex}^{C19} and DCB_{029} for stations outside the BDS flex power coverage area. Similarly, the convergence times of BDS PPP corrected by DCB_{Flex}^{C19} and DCB_{029} were the same for most stations outside the flex power coverage area, and only a few stations had different convergence times. There are three stations in Fig. 15 that do not show data, indicating that their PPP solutions did not converge.

Table 10 presents the percentage of stations that exhibited faster convergence in PPP when corrected with DCB_{Flex}^{C19} and DCB_{029} within and outside the BDS flex power coverage area. The results indicated that 55.0% of the stations within the flex power coverage area experienced faster convergence of BDS PPP when corrected by DCB_{Flex}^{C19}. However, outside the flex power coverage area, 75.0% of the stations exhibited the same convergence time for BDS PPP when corrected

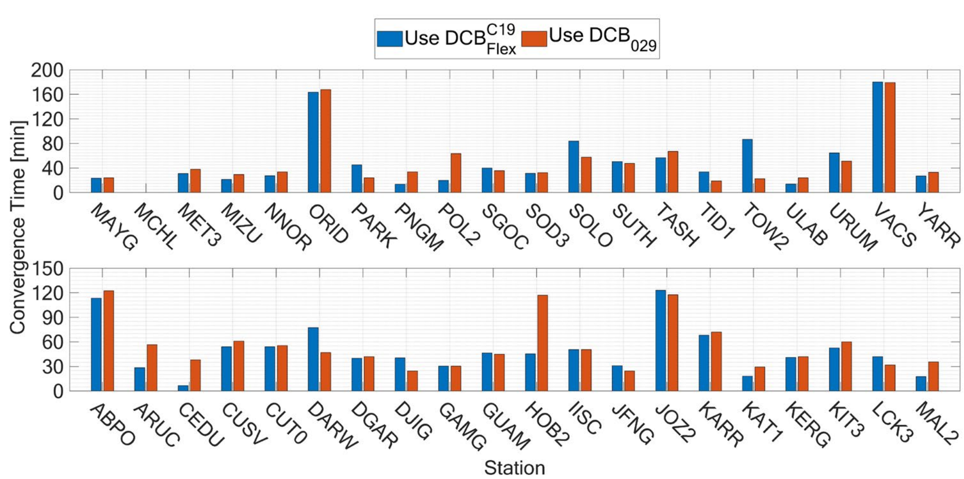

Fig. 13 Convergence time of BDS PPP corrected by DCB_{Flex}^{C19} and DCB_{029} for the stations within the flex power coverage area and data time from 20:00UT to 24:00UT on DOY 029, 2021

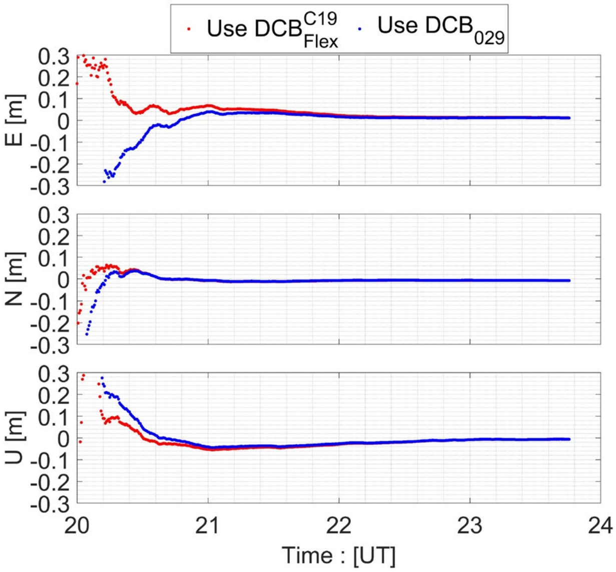

Fig. 14 BDS PPP convergence graphs for the KAT1 station in the E, N, and U directions corrected by DCB^{C19}_{Flex} and DCB_{029} and data time from 20:00UT-24:00UT on DOY 029, 2021

by DCB^{C19}_{Flex} and DCB_{029}. Table 11 presents the maximum, minimum, and average improvement in convergence time of 22 BDS stations that exhibited faster PPP convergence when corrected by DCB^{C19}_{Flex}. The results demonstrated an average improvement in convergence time of approximately 14.0 min.

The two experiments indicated that the correction of daily DCB products DCB_{029} had a significant impact on the PPP convergence time of the stations within the flex power coverage area. When the flex power was activated at part of the day, it resulted in the extension of BDS PPP convergence time for most stations within the flex power coverage area, regardless of whether the flex power was activated. Before and after activation of all satellites' flex power, 67.5% and 55.0% of these stations had extended PPP convergence

Table 10 Number and percentage of stations exhibited faster convergence of BDS PPP using DCB^{C19}_{Flex} and DCB_{029} correction in different regions on DOY 029, 2021

Convergence faster DCB used	Flex power covered		Flex power not covered	
	Number of stations	Percentage	Number of stations	Percentage
Using DCB^{C19}_{Flex}	22	55.0%	2	5.0%
Using DCB_{029}	14	35.0%	5	12.5%
Same	3	7.5%	30	75.0%

Table 11 Maximum, minimum, and average convergence time improvement for stations within the flex power coverage area that showed faster convergence with PPP corrected by DCB^{C19}_{Flex} on DOY 029, 2021

Max		Min		Average
Station	Value [min]	Station	Value [min]	Value [min]
HOB2	− 71.5	KERG, SOD3	− 1.0	− 14.0

time, with an average extension time of 17.9 and 14.0 min, respectively. Therefore, this influence should not be ignored in high-precision positioning.

Conclusion

The flex power technology of GNSS systems can improve the anti-jamming ability of navigation signals by increasing the power of the designed signal. In this paper, the variation characteristics of C/N_0 and daily DCB products during BDS flex power active event occurring at DOY 143–148 in 2022 were examined. The B3I signal of BDS-2's GEO, MEO, and IGSO satellites showed flex power capability, which achieved a 6–10 dB improvement of the final receiver signal. The time series of the C2I–C6I DCB daily product during BDS flex power active period indicates that the activation

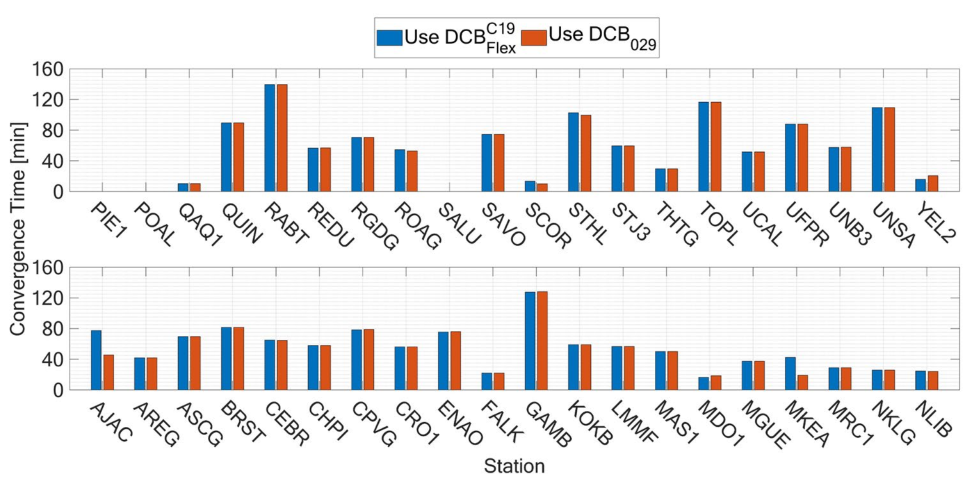

Fig. 15 Convergence time of BDS PPP corrected by DCB^{C19}_{Flex} and DCB_{029} for the stations outside the flex power coverage area and the data time from 20:00UT to 24:00UT on DOY 029, 2021

of BDS flex power led to an increase in DCB for MEO and IGSO satellites, while causing a decrease in DCB for GEO satellites.

To investigate the influence of BDS flex power on DCB estimation, observations of 152 IGS station on DOY 029, 2021 were analyzed. Based on the reference satellite constraint, two DCB estimation strategies, i.e., the high-rate method and the constant method, were applied to the C2I–C6I DCB estimation. Results show that the DCB of the satellites without flex power activated did not change, whereas the DCB of the IGSO satellites with flex power activated increased by 10–15 ns. The BDS flex power caused immediate change above the noise level in the satellite DCB time series. Since BDS flex power was activated at part of the day, the results obtained from the method assuming a constant DCB over a day demonstrated apparent disparities compared to the results estimated by distinguishing DCB into two different constants.

Finally, different DCB corrections were applied in PPP processing. The results revealed that the correction of daily DCB products had a significant impact on the PPP convergence time of the stations within the flex power coverage area. When the flex power was activated at part of the day, it resulted in the extension of BDS PPP convergence time for most stations within the flex power coverage area, regardless of whether the flex power was activated. However, outside the coverage range of IGSO satellites with flex power activated, it did not lead to any prolongation of PPP convergence time.

Acknowledgements We acknowledge CAS and DLR for providing DCB products (https://cddis.nasa.gov/archive/gnss/products/bias). We acknowledge IGS for providing the station data (https://cddis.nasa.gov/archive/gnss). We are grateful to the reviewers for their assistance in evaluating this paper.

Author contributions ZW and SL contributed to the conception of the study. WZ and SL contributed significantly to the data analysis and manuscript preparation. HW and MJ wrote part of the manuscript. PM and SX contributed to some data analysis work.

Data availability The GNSS datasets analyzed during the current study are available from ftp://cddis.gsfc.nasa.gov/pub/.

Declarations

Competing interests The authors declare no competing interests.

References

Cui J (2022) Study on estimation and time-varying characteristics of GNSS differential biases. In: Shanghai Astronomical Observatory, Chinese Academy of Sciences

Dai P, Xing J, Ge Y, Yang X, Qin W, Dong Y, Zhang Z (2021) The effect of BDS-3 time group delay and differential code bias corrections on positioning. Appl Sci 11:104

Esenbuğa ÖG, Hauschild A (2020) Impact of flex power on GPS Block IIF differential code biases. GPS Solut 24:91

Esenbuga ÖG, Hauschild A, Steigenberger P (2020) Impact of GPS flex power on differential code bias estimation for block IIR-M and IIF Satellites. In: Proceedings of the 33rd International Technical Meeting of the Satellite Division of The Institute of Navigation (ION GNSS+ 2020) [C]

Esenbuğa ÖG, Hauschild A, Steigenberger P (2023) Recent flex power changes. GPS Solut 27:104

Ge Y, Zhou F, Sun B, Wang S, Shi B (2017) The impact of satellite time group delay and inter-frequency differential code bias corrections on multi-GNSS combined positioning. Sensors (basel) 17(3):602

Guo F, Zhang X, Wang J (2015) Timing group delay and differential code bias corrections for BeiDou positioning. J Geodesy 89:427–445

Jiménez-Baños D, Perello-Gisbert JV, Crisci M (2010) The measured effects of GPS flex power capability collected on sensor station data. In: 2010 5th ESA Workshop on Satellite Navigation Technologies and European Workshop on GNSS Signals and Signal Processing (NAVITEC)

Li M, Yuan Y, Wang N, Liu T, Chen Y (2018) Estimation and analysis of the short-term variations of multi-GNSS receiver differential code biases using global ionosphere maps. J Geodesy 92:889–903

Li W, Jiao W, Wang K, Qiu R, Sun S (2022) Monitoring and analysis on GPS P(Y) code power enhancement. J B Univ Aeronaut Astronaut 48(11):2193–2203

Montenbruck O, Hauschild A, Steigenberger P (2014) Differential code bias estimation using multi-GNSS observations and global ionosphere maps. J Inst Navig 61(3):191–201

Mou Y, Luo X, Xie Z, Peng X (2023) Performance analysis of four PPP service software under different intensity geomagnetic storms. Adv Space Res 72(5):1593–1604

Ren X, Chen J, Li X, Zhang X (2020) Multi-GNSS contributions to differential code biases determination and regional ionospheric modeling in China. Adv Space Res 65(1):221–234

Steigenberger P, Thölert S, Montenbruck O (2019) Flex power on GPS Block IIR-M and IIF. GPS Solut 23:8

Su K, Jiao G (2023) Estimation of BDS pseudorange biases with high temporal resolution: feasibility, affecting factors, and necessity. Satel Navig 4:17

Tang X, Yuan M, Wang F (2022) Analysis of GPS P(Y) signal power enhancement based on the observations with a semi-codeless receiver. Satel Navig 3:26

Wang N, Yuan Y, Li Z, Montenbruck O, Tan B (2016) Determination of differential code biases with multi-GNSS observations. J Geodesy 90(3):209–228

Wang T, Ruf CS, Gleason S, O'Brien AJ, McKague DS, Block BP, Russel A (2022) Dynamic calibration of GPS effective isotropic radiated power for GNSS-reflectometry earth remote sensing. IEEE Trans Geosci Remote Sens 60:1–12

Xiang Y, Xu Z, Gao Y, Yu W (2020) Understanding long-term variations in GPS differential code biases. GPS Solut 24:118

Yang X, Liu W, Huang J, Xiao W, Wang F (2022) Real-time monitoring of GPS flex power based on machine learning. GPS Solut 26:73

Zhong J, Lei J, Dou X, Yue X (2015) Is the long-term variation of the estimated GPS differential code biases associated with ionospheric variability? GPS Solut 20:313–319

Zhou F (2018) Theory and Methodology of Multi-GNSS Undifferenced Uconmbined Precise Point Positioning. In: East China Normal University

Zhou F, Dong D, Li P, Li X, Schuh H (2019) Influence of stochastic modeling for inter-system biases on multi-GNSS undifferenced and uncombined precise point positioning. GPS Solut 23:1–13

Zhou Wu is currently working toward a MS degree at China University of Geosciences, Beijing. His research primarily focuses on Multi-GNSS PPP and DCB estimation.

Shuhui Li received a PhD degree from China University of Geosciences, Beijing. She is currently the Associate Professor of China University of Geosciences, Beijing. Her current research interests include high-precision GNSS data processing and GNSS ionospheric studies.

Hongxia Wan received her MS degree in Electronic and Communication Engineering from the University of Chinese Academy of Sciences in 2013. Currently, she is an engineer in the China Satellite Network Innovation Co., Ltd., Beijing, China. Her research interests include navigation augmentation and system design.

Ming Ji is currently working toward a MS degree at China University of Geosciences, Beijing. His research primarily focuses on LEO navigation and Doppler positioning.

Pengrui Mao is a MS student currently enrolled at China University of Geosciences, Beijing. His primary research focus revolves around GNSS trustworthy navigation.

Shaojie Xiong is a MS student at China University of Geosciences, Beijing. He is mainly engaged in the research of NLOS signal classification and PPP positioning.